The Astrophysical Journal, 727:32 (10pp), 2011 January 20 doi:10.1088/0004-637X/727/1/32

ASYMMETRIES IN THE EXPANSION AND EMISSION FROM YOUNG SUPERNOVA REMNANTS

Carlos D. Vigh[1,2,4], Pablo F. Velázquez[3], Daniel O. Gómez[1,2,5], Estela M. Reynoso[1,2,5], Alejandro Esquivel[3], and E. Matias Schneiter[3]

[1] Departamento de Física, Facultad de Ciencias Exactas y Naturales de la Universidad de Buenos Aires, Buenos Aires, Argentina
[2] Instituto de Astronomía y Física del Espacio (IAFE), Ciudad Universitaria, C.C.:67, Suc.:28, C.P.: 1428, Buenos Aires, Argentina; carlos@iafe.uba.ar, gomez@iafe.uba.ar, ereynoso@iafe.uba.ar
[3] Instituto de Ciencias Nucleares, Universidad Nacional Autónoma de México, Apdo. Postal 70-543, CP 04510, México D.F., Mexico; pablo@nucleares.unam.mx, esquivel@nucleares.unam.mx; mschneiter@gmail.com
Received 2009 November 26; accepted 2010 November 12; published 2010 December 29

ABSTRACT

We present two-dimensional and three-dimensional numerical simulations of asymmetric young supernova remnants (SNRs) carried out with the hydrodynamical code Yguazú, aiming to quantitatively assess the role of different factors that may give origin to such asymmetries in their expansion. In particular, we are interested in modeling the morphology of Tycho's SNR to address whether the companion star of a Type Ia supernova progenitor has played a role in the subsequent evolution of the remnant. With the results from the numerical simulations, we can not only study the morphology of the SNR but also compute the emission of the remnant in different spectral bands. In particular, we simulate X-ray maps, which can be directly compared to recent and previous observations of Tycho's SNR. Our results suggest that the most likely explanation for Tycho's morphology is that after the supernova (SN) explosion the shock front stripped the envelope of its companion. We represent this effect by adding a conical region with an enhanced density into the initial sphere immediately after the explosion. Assuming that Tycho's companion was a massive red giant star, we explore different values of the angle of aperture and mass excess of the conical region. A good agreement with observational data was found for the model with a mass excess of 0.3 $M_{\odot}$ and an aperture of 90°. After the collision with the SN shock wave, the companion would become an He-rich star. This scenario would gain observational support if a star with these characteristics is found in the vicinity of the center of the SN explosion.

Key words: hydrodynamics – ISM: supernova remnants – methods: numerical – shock waves – supernovae: individual (Tycho)

1. INTRODUCTION

Evolved stars can end their lives in one of the most energetic phenomena known today: a supernova (SN) explosion. Depending on the presence of hydrogen in the light curve, SNe can be broadly classified as Type I and Type II. While SN belonging to most subclasses within this scheme originates in the gravitational collapse of a massive star, a Type Ia SN originates in a binary system when one of its components (the SN progenitor) is a white dwarf (WD) accreting mass from its companion. In this case, the SN explosion takes place when the WD approaches the Chandrasekhar mass. In a Type II SN event, instead, the progenitor is a giant star whose core loses equilibrium and gravitationally collapses while the outer shells are expelled away. The energy released in either of these events will perturb the surrounding interstellar medium (ISM) for a time span that can be as long as tens or hundreds thousand years. As a result of the SN explosion, a shock wave is generated and propagates outward throughout the progenitor's environment. The region enclosed by this shock wave, which contains both the SN ejecta and the swept up material, is known as the supernova remnant (SNR).

Standard evolutionary models of SNRs yield morphologies that are assumed to be spherical. According to the scheme proposed by Woltjer (1972), young SNRs are theoretically expected to undergo a free expansion stage (expansion at constant radial speed) followed by the adiabatic or Sedov expansion stage (in which the radius grows as $t^{2/5}$; Sedov 1959). However, observations of the so-called historical SNRs (such as Tycho's and Kepler's SNRs) exhibit asymmetries both in their morphologies and in their emission patterns (in radio and/or X-rays).

There is increasing interest in the literature to find out the characteristics of the SN progenitors for these young remnants and investigate if they can leave a signature in the subsequent SNR. For instance, if the SN progenitor was a red giant (RG; core-collapse SN explosion), it is expected that the dense and slow wind typically blown by these stars would have modified the density distribution of the surrounding circumstellar medium (CSM) prior to the explosion. This seems to be the case for Kepler's SNR, which will be discussed in Section 2 (see also Velázquez et al. 2006).

The SN explosion witnessed by Tycho Brahe in 1572, on the other hand, is often regarded as the archetype for Type Ia SN. Radio-continuum maps of Tycho's SNR reveal an almost spherical shell with a mean radius of 4′ (Figure 1). However, while the western side of the shell is well defined, the eastern side looks more evolved, with some departure from the spherical shape. An expansion study made by Reynoso et al. (1997), based on high-resolution radio data, shows that the eastern side expands at a lower speed with respect to the western side. Very Large Array (VLA) H I absorption studies toward Tycho's SNR (Schwarz et al. 1995; Reynoso et al. 1999) show a density enhancement to the east. In particular, Reynoso et al. (1999) detect a small H I clump at the location where the expansion velocity is lowest. Lee et al. (2004) report the detection of a CO cloud adjacent to the radio shell, giving further support to the presence of a dense cloud to the east of Tycho's SNR. In X-rays, the western region displays strong emission (e.g., Warren et al. 2005; Vancura et al. 1995). The different expansion rates of the eastern and western regions and the asymmetry

[4] Fellow of Fundación YPF
[5] Member of the Carrera del Investigador Científico, CONICET

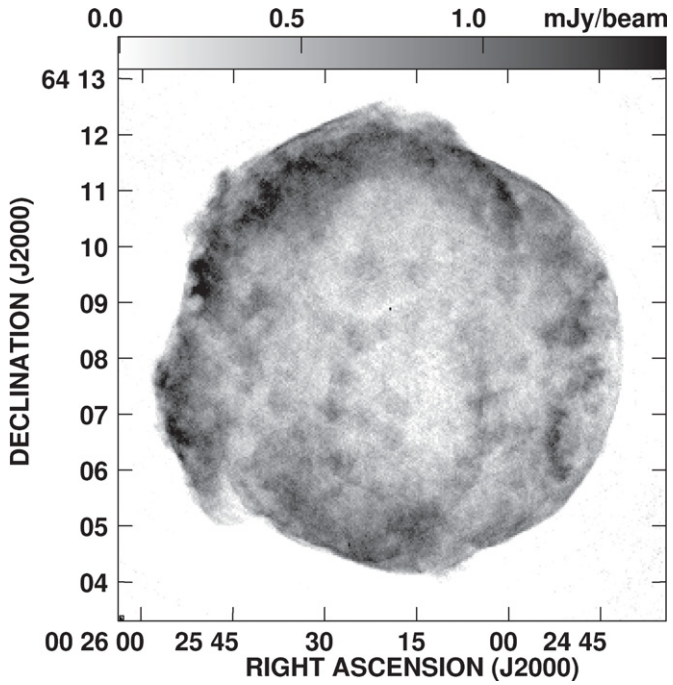

Figure 1. Radio-continuum image of Tycho's SNR at 1315 MHz obtained with the VLA (from Reynoso et al. 1997). The gray scale is indicated at the top of the image. The beam size is $1''.45 \times 1''.38$, and the sensitivity, 140 μJy beam^{-1}.

in the X-ray line emission cannot be explained by standard evolutionary models.

Several attempts have been made to find the surviving companion of Tycho's SN progenitor. Ruiz-Lapuente et al. (2004) proposed a main-sequence star which they called Tycho G as a promising candidate based on its proximity to the geometrical center of Tycho's SNR and its high proper motion and radial velocity. However, González Hernández et al. (2009) note that the rotational velocity is too low and the Ni and Li abundances are too high for Tycho G to be a giant star. Further discussion about the likelihood of Tycho G as the progenitor's companion is given in Kenzendorf et al. (2009), where the authors conclude that the evidence is interesting but not compelling.

The likely companions of Type Ia SN progenitors are main sequence, sub-giant, and RG stars. Marietta et al. (2000; and references therein) studied the result of an SN shock wave that originated in a Type Ia event impacting on the companion star. They find that after the shock wave passes through the companion, part of its upper atmosphere can be entrained into the SN ejecta. We have carried out numerical simulations with the adaptive grid code Yguazú-a (axisymmetric as well as three dimensional) to study how the orbital motion and/or material stripped from a companion star would affect the morphology and evolution of young SNRs. In particular, we analyze the case of Tycho's SNR. In order to compare our numerical results with observations, we have also obtained synthetic X-ray emission maps.

The present paper is organized in the following way. In Section 2, we describe possible causes for asymmetric expansion. The theoretical background is presented in Section 3. In Section 4, we provide the numerical setup and describe the generation of synthetic X-ray emission maps, as well as the overall features of the Yguazú-a code. Our results are presented in Section 5, along with comparisons with observations. Finally, in Section 6 we present our summary and conclusions.

2. POSSIBLE CAUSES FOR ASYMMETRICAL EXPANSION

When a star explodes as an SN, the first evolutionary phase can be regarded as a free expansion, corresponding to a spherical shell whose radius grows linearly with time. When the ISM mass swept up by the expansion becomes comparable to the mass of the progenitor, the deceleration of the expanding front can no longer be neglected. At this stage the remnant evolves adiabatically, according to Sedov's scenario (Woltjer 1972), and the radius expands like $R \propto t^{2/5}$. At a later stage, radiative losses eventually become important and the expansion law changes to $R \propto t^{1/4}$. If the mass of the ISM is homogeneously distributed, the expansion will retain its spherical symmetry. However, in most cases this morphology is not observed. A variety of mechanisms to explain the departures from spherical shapes in young SNRs have been proposed. Below, we list some of the possible causes of asymmetry.

2.1. Inhomogeneous Interstellar Medium

A spatially inhomogeneous mass distribution in the ISM is probably the most obvious cause for an asymmetric expansion of SNRs. For example, the presence of atomic or molecular clouds around the SN site might have a strong effect due to the deceleration of the shock wave when impinging on a denser medium. Also, the decreasing density gradient outward from the Galactic plane may play an important role in shaping an evolved SNR. The degree of asymmetry that can be attained depends on the initial energy of the explosion and the steepness of the density gradient. Examples of this scenario have already been reported in the literature, such as the SNRs 3C 400.2 (Schneiter et al. 2006) and W50 (Zavala et al. 2008).

2.2. Proper Motion of the Progenitor

Let us consider the case where the progenitor star moves with a high velocity with respect to its CSM. If this star is in its RG phase, which is likely to be the case of a Type II SN explosion, there is a dense and slow stellar wind blowing toward its CSM and generating a bubble. As a result of the interaction between this moving isotropic stellar wind and the surrounding medium, a bow shock will develop, giving rise to a cometary structure. In this way, an anisotropy in the density distribution around the progenitor is progressively being built, and when the progenitor explodes, the SN shock wave will propagate through this anisotropic background. Strong departures in both morphology and emission would be observed when the SNR shock reaches the border of the bow shock. This scenario has been found to be appropriate to describe the main features of Kepler's SNR (Bandiera 1987; Borkowski et al. 1992; Velázquez et al. 2006).

2.3. Unbinding a Binary System

In this scenario, the progenitor is a WD that belongs to a binary system. If both stars are sufficiently close to each other, mass can be transferred from the companion (a main sequence, sub-giant, or RG star) to the WD (e.g., Marietta et al. 2000). The total amount of mass transferred can be large enough to break the internal equilibrium of the WD star, triggering its explosion as a Type Ia SN. Assuming that all the mass of the progenitor is ejected in the explosion, the gravitational binding would disappear, in which case the ejecta would receive a "kick" that will separate it progressively from the companion. This

Table 1
Parameters of Possible Companions in Type Ia SN and Corresponding v_k

Stage	$M_2(M_\odot)$	$a_{10}(10^{10}$ cm)	$v_{\rm orb}$(km s^{-1})	v_k(km s^{-1})
MS	1.0	13.8	480	200
SG	1.1	19.2	420	185
SG	2.0	23.2	443	260
RG	1.0	1200.0	51	21

"kick" has a velocity (with respect to the mutual center of mass) $v_k = M_2 v_{\rm orb}/(M_1+M_2)$, where M_1 and M_2 are the progenitor and companion masses, respectively, and $v_{\rm orb}$ is the orbital velocity, given by

$$v_{\rm orb} = 1.16 \times 10^8 \sqrt{\frac{M_1 + M_2}{a_{10}}}\ {\rm cm\ s^{-1}}, \quad (1)$$

where a_{10} is the orbital radius in units of 10^{10} cm and M_1 and M_2 are given in units of $M_\odot$. In Table 1, we show the parameters assumed for a list of possible companion stars and the different values of the "kick" velocity that will be used in our simulations. In all our runs, we assume that the mass of the progenitor M_1 is 1.4 $M_\odot$. The first column indicates the evolutionary stage of the companion star. The second one gives the mass of the companion, the third one lists the orbital radius, the fourth represents the orbital velocity of the reduced mass of the binary system, and the last one is the "kick" velocity.

Another possible consequence of the presence of a companion star is the so-called mass-loading effect that might take place when the expanding shock encounters the companion and strips a fraction of its atmospheric material. We describe the role of this effect on the asymmetry of the SNR in Section 2.5.

2.4. Anisotropic Interior

If the mass distribution of the progenitor's interior is itself anisotropic, the subsequent explosion will be anisotropic as well. This could be the case, for instance, for fast rotating stars.

2.5. Mass Loading Due to the Companion Star

This asymmetry is caused by the impact of the SNR shock wave on the companion star. After this collision, the SNR shock sweeps up material (mass loading) from the upper atmosphere of the companion star. The material is embedded in the SN ejecta, generating an asymmetric density distribution, which would translate into a differential expansion of the remnant. The collision between the shock wave of an SN and its companion star has been studied numerically by Marietta et al. (2000). More recent numerical studies have been performed by Kasen et al. (2004) and Pakmor et al (2008). All these studies focus on the first stages after the collision between the SN shock and the companion star (from a few days up to a few months), where physical processes other than the mass loading are also relevant. Marietta et al. (2000) find that if the companion is a main-sequence star it can lose about 15% of its mass, while an RG companion can lose up to 98% of its envelope. Since the amount of mass stripped from the companion can be an appreciable fraction of the total mass of the progenitor's mass, we believe that this can be an adequate scenario for Tycho's SNR.

3. THEORETICAL BACKGROUND

In this section, we briefly review the theoretical background of SNR evolution, keeping in mind that we are mostly interested in young remnants. We also consider the effects of the inhomogeneities of the ISM and proper motion of the progenitor due to the disruption of a binary system.

3.1. Free Expansion and Sedov SNR Evolutionary Phases

We are interested in studying the evolution of Type Ia SNe, such as Tycho's SNR. The initial evolution of this kind of remnant is usually described considering that by the time of the SN explosion, the inner 4/7 of the total ejected mass has a constant density ρ_c up to a radius r_c, while the remaining outer 3/7 of the ejected mass follows a power-law density $\rho \sim r^{-7}$ (Colgate & McKee 1969; Chevalier 1982; Jun & Norman 1996).

Under this assumption, Truelove & McKee (1999) obtained approximate shock trajectories for the free expansion and adiabatic phases, which are given by

$$R_b^* = 1.06\, t^{*4/7} \quad (2)$$

for the free expansion phase and

$$R_b^* = (1.42\, t^*\ - 0.321)^{2/5} \quad (3)$$

for the adiabatic or Sedov–Taylor phase. In Equations (2) and (3), $R_b^* = R_b/R_{\rm ch}$ is a dimensionless SNR radius and $t^* = t/t_{\rm ch}$ is a dimensionless time, defined by characteristic length and timescales, respectively, given by (Truelove & McKee 1999)

$$R_{\rm ch} = 3.07 \left(\frac{M_*}{n_0}\right)^{1/3}\ {\rm pc} \quad (4)$$

and

$$t_{\rm ch} = 423\ \frac{M_*^{5/6}}{n_0^{1/3}\ E_{51}^{1/2}}\ {\rm yr}, \quad (5)$$

where $M_\star$ is the ejected mass in units of $M_\odot$, n_0 is the unperturbed ISM particle density in cm^{-3}, and E_{51} is the initial energy explosion in units of 10^{51} erg.

The transition from the free expansion to the Sedov–Taylor phase occurs when the amount of swept up mass is larger than the ejected mass. Truelove & McKee (1999) estimated this transition to occur at a time

$$t_{\rm ST} = 0.732\ t_{\rm ch}\ {\rm yr} \quad (6)$$

and a radius

$$R_{\rm ST} = 0.881\ R_{\rm ch}\ {\rm pc}. \quad (7)$$

Depending on whether the remnant is in the free expansion or in the Sedov–Taylor phase, it is possible to obtain an estimate for E_{51} combining Equation (2) or Equation (3) with Equations (4) and (5) for historical SNRs because their ages t_f are known and their radii R_f can be inferred. To this end, a value for the ISM particle density n_0 needs to be assumed, which will be one of the inputs of our numerical simulations. It is straightforward to show that E_{51} is given by

$$E_{51} = 2.9 \times 10^4 (n_0\ M_\star)^{1/2}\ \frac{R_f^{7/2}}{t_f^2} D_3^2 \quad (8)$$

if the remnant is in the first phase of evolution or by

$$E_{51} = 8.9 \times 10^4\ \frac{M_\star^{5/3}}{t_f^2\ n_0^{2/3}} \left[6.05 \times 10^{-2}\ R_f^{5/2} \left(\frac{n_0}{M_\star}\right)^{5/6} + 0.321\right]^2 D_3^2 \quad (9)$$

Table 2
Estimate of Initial Energy Explosion and Initial Radius for the Sedov–Taylor Phase for Different Input Parameters

$n_0(\mathrm{cm}^{-3})$	$M_\star(M_\odot)$	R_{ST}(pc)	t_{ST}(yr)	$E_{51}(10^{51}$ erg)
0.5	1.4	3.8	516	1.0
0.5	1.7	4.1	579	1.1
0.5	2.0	4.3	634	1.2
1.0	1.4	3.0	346	1.4
1.0	1.7	3.2	380	1.6
1.0	2.0	3.4	423	1.7

if the SNR is in the Sedov–Taylor phase. In Equations (8) and (9) t_f is the SNR's age given in years and R_f is the radius given in pc. The distance to Tycho's SNR is ill constrained and still in debate, with values ranging from 1.5 to 4.5 kpc (e.g., Chevalier et al. 1980; Albinson et al. 1986; Schwarz et al. 1980, 1995; Smith et al. 1991; Ruiz-Lapuente et al. 2004). As a working hypothesis, we shall adopt an intermediate value of 3 kpc throughout this paper, which is coincident with the distance suggested by Ruiz-Lapuente et al. (2004). In Equations (8) and (9), $D_3 = D(\mathrm{kpc})/3$ kpc is a correction factor if a different distance to the source is assumed. In Table 2, we use different values of ISM density (Column 1) and total ejected mass (WD and companion's envelope, Column 2) to compute the radius of the shell, R_{ST}, at the beginning of the Sedov phase (Column 3), the transition time to the Sedov phase (Column 4), and the initial energy of the explosion (Column 5). In all cases, the final age is 440 years and the final radius 3.5 pc, which is estimated assuming a distance of 3 kpc.

The effects of deceleration of the forward SNR blast wave due to the acceleration of cosmic rays have not been considered when deriving Equations (8) and (9). This effect can be observationally studied through the relative location between the forward shock and the contact discontinuity. Warren et al. (2005) carried out this analysis for the case of Tycho's SNR and reported evidence in support of this process. Similar results were reported by Miceli et al. (2009) for the case of SN 1006. Recently, Ferrand et al. (2010) have shown that this mechanism can produce a difference of the order of 14 arcsec in the whole expansion of a remnant such as Tycho. This process appears to have a global effect on the SNR dynamics but it cannot explain the observed asymmetries. Besides, it is not clear how much of the initial energy is spent in accelerating particles at the main shock. For these reasons we have not taken into account this effect in our study.

3.2. ISM Density Gradient Versus Kick Scenarios

In this section, we compare two basic sources of asymmetry: a kick velocity, v_k, and a gradient in the ISM density of the form $n_{\mathrm{ISM}}(x) = n_0 \exp(-\mathrm{x/H})$, where x is a Cartesian coordinate with its origin at the remnant center and H is a density scale length. We can think of v_k as a perturbation to the expansion velocity profile that translates into an energy perturbation E_1, i.e., $E \simeq 0.5\, m\, (v_0\, \hat{r} + v_k \hat{x})^2 \sim E_0 + E_1$, where $E_0 = 0.5\, m\, v_0^2$ and $E_1 = m\, v_0\, v_k \cos\theta$ (θ is the angle between the expansion velocity and the "kick" direction). The relative importance between these two effects can be evaluated taking into account Equations (2) and (3). The perturbation caused by both effects can be written as (see also Equation (5))

$$E^{1/2} n_{\mathrm{ISM}}^{1/3} \approx E_0^{1/2} n_0^{1/3} (1+\epsilon_k)(1-\epsilon_n) \approx E_0^{1/2} n_0^{1/3} (1+\epsilon_k-\epsilon_n)\,, \quad (10)$$

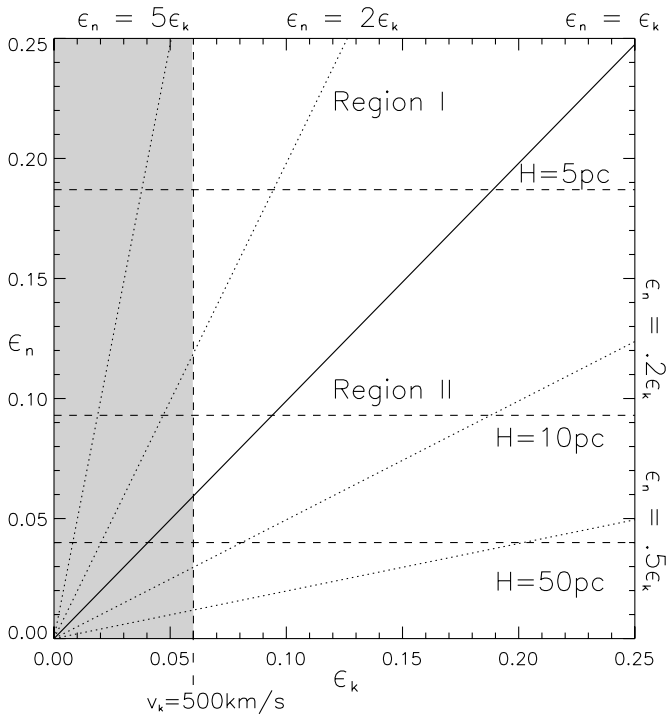

Figure 2. Phase map where the vertical axis represents perturbations to the expansion radius due to density gradients and the horizontal axis represents perturbations by kinematical effects. Region I is the zone dominated by density anisotropies, and region II by the effects of the "kick." We will focus on the particular cases limited within the gray region.

where $\epsilon_k = v_k \cos\theta / v_0$ and $\epsilon_n = x/3H$. Therefore, replacing Equation (10) into Equation (2), we obtain

$$(R_b^*)^{7/4} \approx 2.6 \times 10^{-3} \frac{E_{51}^{1/2}\, n_0^{1/3}\, t}{M_*^{5/6}}\, [1 + (\epsilon_k - \epsilon_n)]\,. \quad (11)$$

Based on Equation (11), it is possible to assess which of the two effects is quantitatively more important: the kick (characterized by ϵ_k) or the density gradient (described by ϵ_n). As a result of either ϵ_k or ϵ_n, $R_S(t)$ in any given direction could depart from the symmetric case. Figure 2 shows the relative importance between ϵ_n and ϵ_k. The solid straight line represents the condition $\epsilon_k = \epsilon_n$, corresponding to comparable effects between the kick and the ISM density gradient. In region II, the asymmetries are dominated by the kick velocity, while region I shows the zone where anisotropies due to a density gradient are more important. Density gradients can arise, for example, in the presence of local molecular clouds or in a turbulent ISM. The gray area in Figure 2 displays the region of kick velocities smaller than 500 km s^{-1}, which is a reasonable assumption for an SNR like Tycho. We find that even for relatively large values of v_k, between 100 km s^{-1} and 500 km s^{-1}, and for reasonably mild density gradients characterized by H between 5 pc and 50 pc, the most important cause of asymmetry is the density gradient.

3.3. Asymmetric Explosion Due to the Companion Star: A Simple Model

To allow for the mass-loading effect described in Section 2.5, our simplified model assumes that shortly after the explosion, the mass distribution is given by two axisymmetric cone-shaped regions, each one with a homogeneous density distribution, as

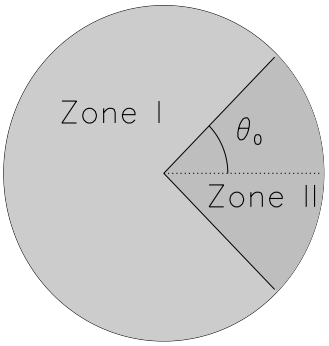

Figure 3. Scheme showing the initial configuration for the asymmetric explosion case due to the extra material from the companion star. Zone I represents the region that has only mass from the progenitor, and Zone II the region with progenitor mass and the excess due to its companion.

sketched in Figure 3. We calculated the total energy and mass for such a density distribution, while maintaining the center of mass at rest. Zone I contains only material from the progenitor star, while Zone II also includes the extra mass provided by the outer envelope of the companion, after the main SNR shock wave collides with it. We have the following set of equations for mass, energy, and momentum:

$$\begin{cases} M & = & M_I + M_{II} & = & \frac{1}{2}M_0(1+\cos\theta) + \frac{1}{2}M_0(1-\cos\theta)\epsilon^{-1} \\ E & = & E_I + E_{II} & = & \frac{1}{2}E_0(1+\cos\theta) + \frac{1}{2}E_0(1-\cos\theta)\epsilon^{-1} \\ \rho_I v_I & = & \rho_{II} v_{II} & \Rightarrow & v_I = \epsilon v_{II} \end{cases}, \quad (12)$$

where we define the total energy as $E_0 = \frac{2}{5}\pi r_{\rm in}^3 \rho_I v_I^2$, the mass as $M_0 = \frac{4}{3}\pi r_{\rm in}^3 \rho_I$, and the density contrast as $\epsilon = \frac{\rho_{II}}{\rho_I}$. The mass excess, $m_{\rm exc} = \frac{1}{2}M_0(1-\cos\theta)(\epsilon - 1)$, is included in M_{II} where we have assumed $\epsilon \geqslant 1$. Additional parameters are $r_{\rm in}$, the initial radius considered, and the aperture of the cone θ_0. For $\epsilon = 1$, the problem reduces to the symmetric case with $E = E_0$ and $M = M_0$. We perform simulations with three different masses: 1.4 $M_\odot$ for the symmetric explosion case, 1.7 $M_\odot$ and 2 $M_\odot$ for the models that include a binary system with a massive companion.

4. NUMERICAL SIMULATION

4.1. Initial Setup and Code Description

The hydrodynamic numerical simulations shown in this work were carried out with the two-dimensional axisymmetric and a full three-dimensional version of the adaptive mesh Yguazú-a code, which is described in detail by Raga et al. (2000).

In this code, the gasdynamic equations are integrated with a second-order accurate (in space and time) implementation of the "flux-vector splitting" algorithm of van Leer (1982). A system of rate equations for atomic/ionic species is also integrated together with the gas dynamic equations. With these chemical equations, it is possible to compute a non-equilibrium cooling function (with a parameterized cooling rate applied for the high-temperature regime). Rate equations for H I II, He I III, C II IV, and O I IV are considered. The reaction and cooling rates which have been included are described in more detail in Raga et al. (2002) and Raga et al. (2007).

For the two-dimensional axisymmetric simulations, a five-level binary adaptive grid with a maximum resolution of 3×10^{16} cm was used, in a 10 pc × 5 pc (axial × radial) computational domain. The three-dimensional simulations are also done in a five-level binary adaptive grid but with a maximum resolution of 6×10^{16} cm. A cubic computational domain was considered with a physical size of 10 pc along each Cartesian direction.

As mentioned above, our main goal is to model an SNR with the characteristics of Tycho's SNR. The average radius of this remnant is ∼3.5 pc if a distance of 3 kpc is considered (Section 3.1), and its age is 440 years. If a number density n_0 of 0.5 cm^{-3} is assumed, from Table 2 and Equation (8), we derive a value of $E_0 = 10^{51}$ erg for the initial SN energy explosion. This value is in agreement with previous estimates given by Badenes et al. (2006). Employing detailed one-dimensional simulations, Badenes et al. (2006) showed that delayed detonation models with kinetic energies around 10^{51} erg can reproduce the fundamental properties of the X-ray emission from the shocked SN ejecta, constraining the explosion of SN 1572 to be a normal Type Ia. In addition they were also able to reproduce some morphological characteristics, such as the positions of the reverse shock and contact discontinuity. This has later been confirmed by the light echo spectrum presented in Krause et al. (2008). Using these values for n_0 and E_0 in Equations (6) and (7), we find that the remnant is close to finish its free expansion phase (see Table 2).

The SNR was initialized by applying radial velocities to a sphere of radius 6.2×10^{17} cm (21 cells in the finest grid) for the axisymmetric simulations, centered along the symmetry axis at $x = 5$ pc and $r = 0$, where a reflective boundary condition is imposed. For the fully three-dimensional simulations, the energy is placed into a sphere of radius 10^{18} cm (equivalent to 16 pixels at the maximum resolution), centered on a cubic Cartesian domain.

For the "kick" models (where the ejecta acquires an extra velocity due to the orbital motion of the progenitor when it explodes as a Type Ia SN), we integrate the hydrodynamic equations in the reference frame of the progenitor. This condition is equivalent to assuming that the ISM, with $n_0 = 0.5\,{\rm cm}^{-3}$ and a temperature of 10^3 K, moves with a velocity $v_{\rm ISM} = -v_k$. According to Table 2, we choose "kick" velocities of 0, 200, and 500 km s^{-1}. Furthermore, we assume that an initial mass for the ejecta ($M_\star$) of 1.4 $M_\odot$ is uniformly distributed within the initial remnant radius, i.e., the initial remnant density is constant. The velocity was modeled with a linear profile, with a maximum velocity at the initial SNR radius given by $v_{\rm max} = \sqrt{\frac{10}{3}E_k/M_\star}$. The initial kinetic energy, E_k, was set as 95% of E_0, while the remaining 5% was imposed as thermal energy.[6]

To model an asymmetric explosion due to a mass excess from the companion, we initialize the internal structure of the SN as shown in Figure 3 and Equation (12), for both our two-dimensional and three-dimensional simulations considering mass excesses of 0.3 $M_\odot$ and 0.6 $M_\odot$. For the three-dimensional simulations, in order to break the axisymmetry, we impose a fractal density distribution with a spectral index of $-11/3$, which is consistent with the turbulent ISM (see Esquivel & Lazarian 2005; Esquivel et al. 2003; Ossenkopf et al. 2006). The fractal density was imposed on the entire computational domain and has an amplitude of fluctuations on the order of 20% of the mean value.

[6] We also carried out numerical simulations using the initial setup of Type Ia SN given by Jun & Norman (1996). We found that after 440 years both initial setups give similar SNR radii, with difference of the order of 1% (i.e., a difference of 3 arcsec).

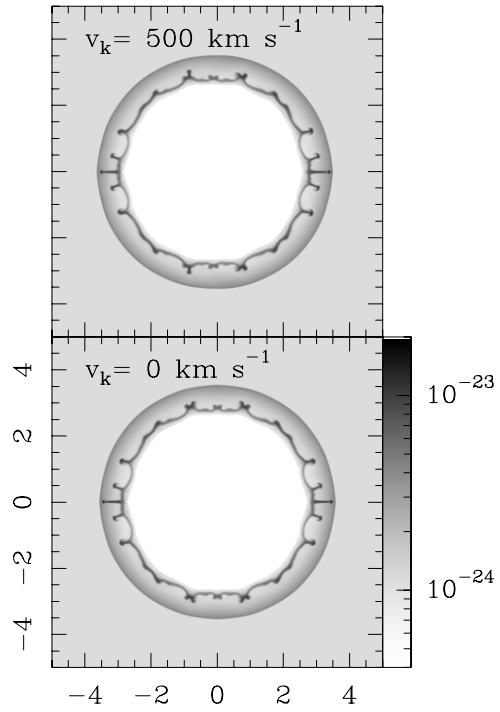

Figure 4. Density map distribution for the cases with a $v_{\rm kick}$ of 500 km s^{-1} (top panel) and 0 km s^{-1} (bottom panel). These maps were obtained for an integration time of 440 years. Both axes are given in units of pc. The vertical bar on the right of the bottom panel gives the logarithmic scale of the density, in units of g cm^{-3}.

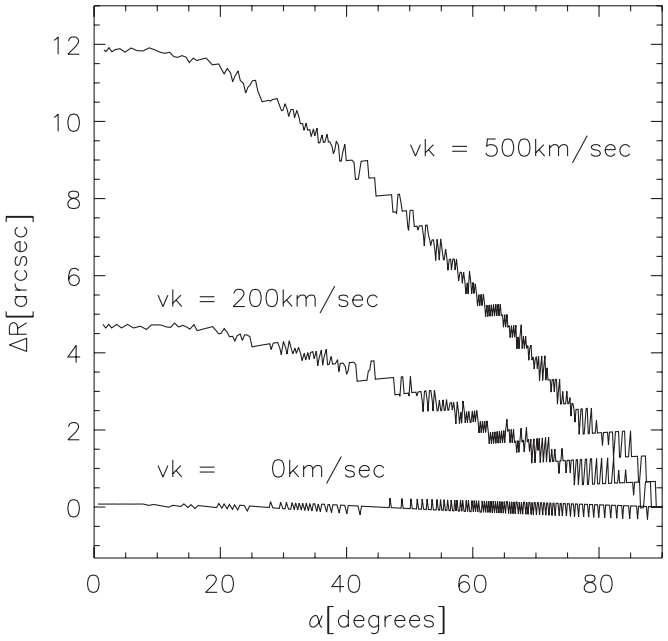

Figure 5. Differential expansion for the case with v_k: 500, 200, and 0 km s^{-1}. The curves display the difference ΔR between radii in the first and second quadrants as explained in Section 4. The vertical axis is ΔR translated to arcseconds, assuming a distance of 3 kpc, in order to compare our theoretical results with observations of Tycho's SNR. The horizontal axis is the azimuthal angle in degrees.

4.2. Simulating the Thermal X-ray Emission

To compare the results arising from our simulations against observations, we also generated synthetic X-ray emission maps.

In the low-density regime, the emission coefficient is calculated as $j_\nu(n, T) = n^2\eta(T)$, where n and T are the particle density and temperature distributions obtained from the numerical simulations. The function $\eta(T)$ depends smoothly on T and is computed over the energy band (0.3–1.6) keV using the CHIANTI[7] atomic database and its associated IDL software (Dere et al. 1997, 2009), where the X-ray spectrum can be fitted with a thermal plasma model, considering both the line and free–free emission. Furthermore, the effects of the interstellar extinction (considering the extinction curve of Morrison & McCammon 1983) have been taken into account. We used the ionization equilibrium (IEQ) model developed by Mazzotta et al. (1998) (also Landini & Fossi 1991) and the element abundances given by Vancura et al. (1995).

5. RESULTS AND DISCUSSION

We first tested the effect of an explosion in a uniform ISM where the ejecta receives a kick originated in the breakup of the binary system. We carried out three runs for the following values of v_k: 0, 200, and 500 km s^{-1} (see Table 1). In these models, the remnant was kept at rest at the center of the computational domain, while the ISM moves with v_k in the $-\hat{x}$ direction. The resulting density stratification maps for the two extreme cases at an age of 440 years are shown in Figure 4. These maps show virtually no difference between them: the positions of the shock front and even the Rayleigh–Taylor (RT) finger pattern are almost identical.

In order to perform a more detailed study of the expansion, we proceed as follows: in our numerical results we measure the radius as a function of angular position in the first quadrant and do the same in the second quadrant. Then, we compute the difference ΔR between pairs of radial distances taken at α and $180^\circ - \alpha$, where α is the azimuthal angle measured counterclockwise from the $+x$ direction. For $\alpha = 90^\circ$, both radii are of course coincident, while at $\alpha = 0^\circ$, the difference attains its maximum value (see Figure 5). For the extreme case $v_k = 500$ km s^{-1}, a difference of up to 13 arcsec is obtained. For the intermediate case, $v_k = 200$ km s^{-1}, this difference reduces to 6 arcsec. These results show that this mechanism actually produces a differential expansion, but it is quantitatively insufficient to explain the degree of departure from spherical symmetry observed in Tycho's SNR. Regardless of the actual location of the center of the explosion, we estimate the degree of asymmetry in Tycho's SNR to be of the order of $\Delta R \approx 40$ arcsec.

Another mechanism that we explored was an inhomogeneous ISM, characterized by exponential density gradients with different intensities. Since Tycho's SNR is expanding into a molecular cloud to the east (Lee et al. 2004; Cai et al. 2009), we modeled the ISM with a density gradient that spanned from 0.1 cm^{-3} (typical density for the diffuse ISM) to 10^3 cm^{-3} (typical density of a molecular cloud) within a scale length equivalent to half the width of the computational domain, i.e., 5 pc. The result was an elongated SNR with the brighter, smaller hemisphere closer to the molecular cloud, similar to that observed and modeled for the case of the Magellanic SNR N120 (Reyes-Iturbide et al. 2008). However, the direction of the elongation and emission enhancement observed in Tycho's SNR is opposite the predictions of the model. For these reasons we discard this mechanism as the source of asymmetry of Tycho's SNR.

[7] The 6.0.1 version of the CHIANTI database and its associated IDL procedures are freely available at: http://www.arcetri.astro.it/science/chianti/chianti.html and http://www.chiantidatabase.org/chianti_download.html

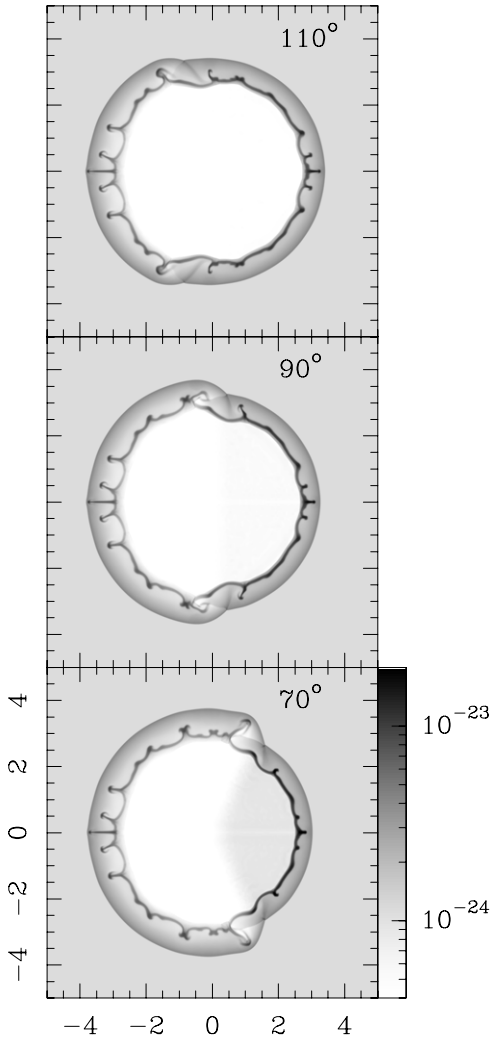

Figure 6. Density map distribution for the case of a mass excess of 0.3 $M_\odot$ considering aperture cone angles of 110° (top panel), 90° (central panel), and 70° (bottom panel). The morphology of the 90° case resembles that of Tycho's SNR.

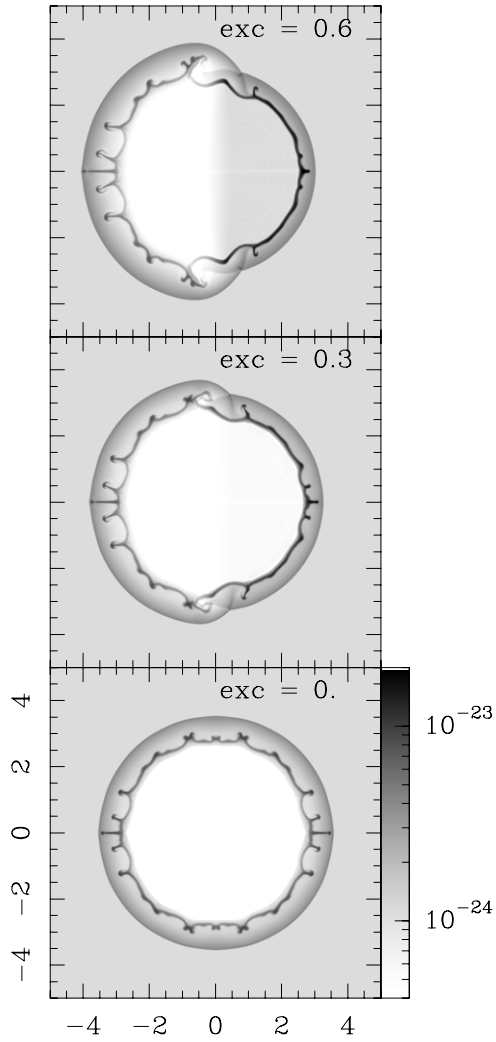

Figure 7. Density stratification for a fixed aperture angle of 90° with different values of mass excess. A mass excess of 0.6 $M_\odot$ (top panel), 0.3 $M_\odot$ (middle panel), and no excess (bottom panel). These maps were obtained for an integration time of 440 years. Both axes are given in pc. The vertical bar on the right of the bottom panel gives the logarithmic scale of the density, in units of g cm^{-3}.

Alternatively, we analyze the influence of the material from the companion star on the remnant expansion. For that purpose, we carried out three runs considering a mass excess of 0.3 $M_\odot$ and different aperture angles θ_0: 70°, 90°, and 110°. Figure 6 displays density stratification maps for these cases. There is a clear difference between the expansion of the right and left sides in all three cases. The case with $\theta_0 = 90°$ exhibits both a good morphological agreement with the radio-continuum images of Tycho's SNR and a radius difference ΔR of 38 arcsec, which is comparable with the observed one. Keeping $\theta_0 = 90°$, we explored the cases with mass excess of 0.3 $M_\odot$ and 0.6 $M_\odot$. Their density maps are shown in Figure 7. The difference in the expansion radius between the opposite sides reveals that models with mass excesses between 0.3 $M_\odot$ and 0.6 $M_\odot$ are good candidates to explain the differential expansion of Tycho's SNR (see Figure 8).

Based on these axisymmetric numerical results, we generated synthetic X-ray emission maps to compare with X-ray observational data obtained with *Chandra* in 2000. These maps are displayed in Figure 9 and correspond to an integration time $t = 440$ yr. The bottom panel of this figure shows the case when the symmetry axis lies on the plane of the sky, while the top panel represents the map when the symmetry axis is tilted 25° with respect to the plane of the sky. We note that the pattern of the RT fingers observed in the density stratification maps turns into annular structures in the synthetic X-ray maps. These annular structures are artifacts introduced by the process of constructing maps from axisymmetric simulations.

In order to avoid these artifacts, we performed three-dimensional numerical simulations for the case $\theta_0 = 90°$ and a mass excess of 0.3 $M_\odot$. To break the axisymmetry of the problem, we set the remnant to evolve into a medium with a fractal density structure, consistent with a turbulent ISM. The result is shown in Figure 10, which displays the density distribution on the xz and yz planes across the center of the remnant. The distribution of the RT fingers looks very different on both projections. X-ray simulated maps were also generated from this three-dimensional simulation, considering xz and yz projections. These synthetic maps, shown in Figure 11, were performed considering an angle of 25° between the x axis (y axis) and the plane of the sky for the xz projection (yz projection). In this case, the RT fingers develop into entangled bright X-ray filaments, resulting in a clumpy or patchy appearance. Such bright filaments, and an enhancement in the X-ray emission, are observed on the right side of the simulated map.

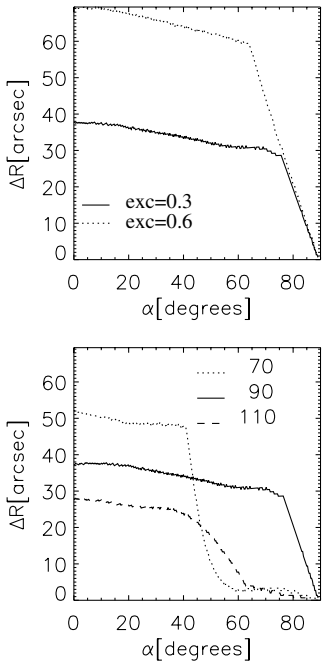

Figure 8. Bottom: comparison of the differential expansion for the cases with a mass excess of 0.3 $M_{\odot}$, considering different aperture cone angles. The lines represent the difference ΔR between radii of the right and left part of the SNR shock. The vertical axis is the radius difference in units of arcseconds (assuming a distance of 3 kpc for Tycho's SNR). The horizontal axis is the azimuthal angle in degrees. Top: idem, but for the case where the aperture of the cone is 90°, considering mass excesses of 0.3 $M_{\odot}$ and 0.6 $M_{\odot}$.

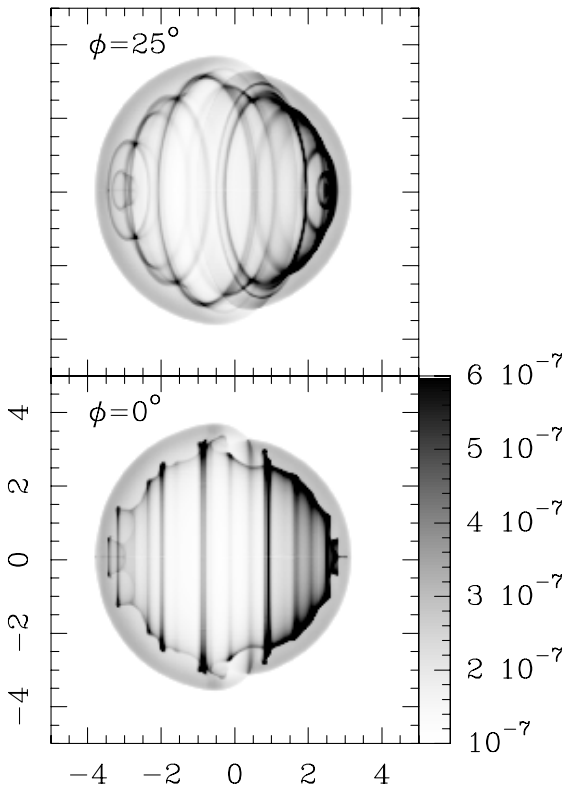

Figure 9. Synthetic X-ray emission maps obtained for the case of an excess mass of 0.3 $M_{\odot}$ and an aperture angle of 90°. The X-ray emission corresponds to the energy band 0.3–1.6 keV. The bottom panel shows the X-ray energy flux when the symmetry axis is on the plane of the sky, while the top panel shows the resulting X-ray map when the symmetry axis is tilted 25° with respect to the plane of the sky. Both axes are given in pc and the vertical bar shows the linear gray scale of the X-ray emission in units of erg s^{-1} cm^{-2} sr^{-1}.

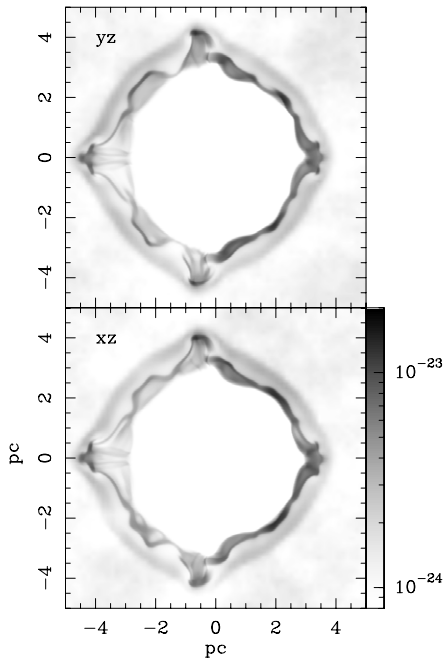

Figure 10. Density distribution maps for the case of an excess mass of 0.3 $M_{\odot}$ and an aperture angle of 90°, obtained from a three-dimensional simulation and an integration time of 440 years. The top panel displays the density distribution on the yz plane, while the bottom panel shows the density on the xz plane, both passing through the remnant center. Both axes are given in units of pc, while the vertical bar on the right of the bottom panel shows the logarithmic scale of the density, in units of g cm^{-3}.

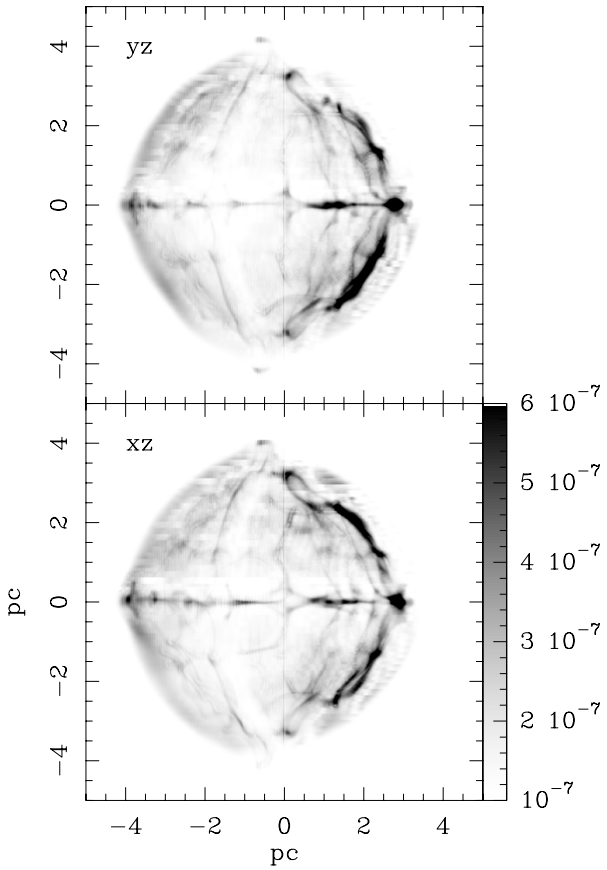

Figure 11. X-ray emission maps for the three-dimensional simulation. The line of sight is tilted by 25° with respect to the plane of the sky and the x-axis (top panel) or the y-axis (bottom panel). Both axes are given in pc while the vertical bar on the right of the bottom panel gives the linear gray scale of the X-ray emission in erg s^{-1} cm^{-2} sr^{-1}.

It must be kept in mind that the method to construct simulated X-ray maps through the CHIANTI database makes use of IEQ models, which are an approximation for the case of young SNRs, because it provides a lower limit to the total X-ray flux (Schneiter et al. 2010). Also, note that the element abundances that we use are those from Vancura et al. (1995), which are not complete. Therefore, our results are not suitable for quantitative comparisons with observations. Nevertheless, it is striking that our simulations (Figure 11) and the X-ray images obtained with *ROSAT*, *Einstein* (Vancura et al. 1995), and *Chandra* (Warren et al. 2005) all display an incomplete arc of enhanced intensity to the west. Also, Vancura et al. (1995) associated this X-ray emission asymmetry with an anisotropic element distribution of the SN ejecta. This result is consistent with our scenario, since this kind of element distribution can be produced by the stripped material from the companion star. Spectral analyses of the X-ray data show that this emission arises in shocked ejecta. According to *Chandra* observations (see Figure 1, bottom right, in Warren et al. 2005), the FeKα line is a major component of this emission. A better determination of the actual abundances in Tycho's SNR, supplied by an increased amount of observational data, will certainly help simulate the X-ray emission with improved accuracy.

6. CONCLUDING REMARKS

The main goal of this study has been to consider different potential causes for the asymmetric expansion observed in many young SNRs. In this paper, we focused our attention on Tycho's SNR. We performed several numerical simulations to assess whether inhomogeneities in the ISM or the existence of a companion of Tycho's progenitor can have any appreciable effect on the subsequent evolution of the remnant.

The most obvious cause of asymmetry in SNRs is the presence of an inhomogeneous ISM in the surroundings of the progenitor. However, for the particular case of Tycho and considering the distribution of molecular clouds in its vicinity, we find that it cannot be the cause for the observed asymmetry.

Considering that Tycho's progenitor was part of a binary system, the companion star might have produced two effects in the expansion of the SNR shell: a kick (of the order of the orbital velocity of the progenitor) as a result of the breakup of the binary system after the explosion and the mass-loading effect of the atmospheric material of the companion. For a range of reasonable orbital parameters, we find that the addition of a velocity kick to the expanding shell produces a negligible effect for the case of Tycho's SNR. The mass-loading effect, on the other hand, might lead to asymmetries comparable to those observed, provided that we assume a swept-up mass between 0.3 and 0.6 solar masses. This scenario is consistent with the companion being in an RG stage by the time of the explosion (see Marietta et al. 2000; Wheeler et al 1975), which does not give support for the hypothesis of Tycho G as the companion star of Tycho SN. This kind of scenario is called the WD+RG (white dwarf plus red giant) channel and is suggested as a likely mechanism for producing SN Ia explosions (Meng et al. 2009; Hachisu et al. 2007; Hachisu & Kato 2006). Moreover, after its envelope is stripped by the SN shell in its expansion, the companion should become an He-rich star (as discussed by Marietta et al. 2000). The finding of such a star among the companion candidates of Tycho's progenitor will certainly provide a strong support to the scenario presented in this paper.

The authors thank the anonymous referee for very useful comments and suggestions. C.V. is supported by a fellowship of Fundación YPF. We acknowledge partial support from PICT 33370/2005 from ANPCyT (Argentina) to IAFE. E.M.R. is partially supported by grants UBACyT X482, PIP 114-200801-00428 (CONICET), and ANPCYT-PICT-2007-00902. P.F.V. and A.E. acknowledge support from grants CONACyT 61547, 101356, and 101975, and DGAPA-UNAM IN119709. The authors also thank Enrique Palacios (ICN-UNAM) for maintaining and supporting our Linux clusters. CHIANTI is a collaborative project involving the NRL (USA), the Universities of Florence (Italy) and Cambridge (UK), and George Mason University (USA).

REFERENCES

Albinson, J. S., Tuffs, R. J., Swinbank, E., & Gull, S. F. 1986, MNRAS, 219, 427
Badenes, C., Borkowski, K., Hughes, J., Hwang, U., & Bravo, E. 2006, ApJ, 645, 1373
Bandiera, R. 1987, ApJ, 319, 885
Borkowski, K. J., Blondin, J. M., & Sarazin, C. L. 1992, ApJ, 400, 222
Cai, Z.-Y., Yang, J., & Lu, D.-R. 2009, Chin. Astron. Astrophys., 33, 393
Chevalier, R. A. 1982, ApJ, 258, 790
Chevalier, R. A., Kirshner, R. P., & Raymond, J. C. 1980, ApJ, 235, 186
Colgate, S. A., & McKee, C. 1969, ApJ, 157, 623
Dere, K. P., Landi, E., Mason, H. E., Monsignori Fossi, B. C., & Young, P. R. 1997, A&AS, 125, 149
Dere, K. P., Landi, E., Young, P. R., Del Zanna, G., Landini, M., & Mason, H. E. 2009, A&A, 498, 915
Esquivel, A., & Lazarian, A. 2005, ApJ, 631, 320
Esquivel, A., Lazarian, A., Pogosyan, D., & Cho, J. 2003, MNRAS, 342, 325
Ferrand, G., Decourchelle, A., Ballet, J., Teyssier, R., & Fraschetti, F. 2010, A&A, 509, L10
González Hernández, J. I., Ruiz Lapuente, P., Fillipenko, A. X., Foley, R. J., Gal-Yam, A., & Simon, J. D. 2009, ApJ, 691, 1
Hachisu, I., & Kato, M. 2006, ApJ, 642, L53
Hachisu, I., Kato, M., & Luna, G. J. M. 2007, ApJ, 659, L153
Jun, B.-I., & Norman, M. L. 1996, ApJ, 465, 800
Kasen, D., Nugent, P., Thomas, R. C., & Wang, L. 2004, ApJ, 610, 876
Kenzendorf, W. E., Schmidt, B. P., Asplund, M., Nomoto, K., Podsiadlowski, Ph., Frebel, A., Fesen, R. A., & Yong, D. 2009, ApJ, 701, 1665
Krause, O., Tanaka, M., Usuda, T., Hattori, T., Goto, M., Birkmann, S., & Nomoto, K. 2008, Nature, 456, 617
Landini, M., & Fossi, B. C. M. 1991, A&AS, 91, 183
Lee, J.-J, Koo, B.-C., & Tatematsu, K. 2004, ApJ, 605, L113
Marietta, E., Burrows, A., & Fryxell, B. 2000, ApJS, 128, 615
Mazzotta, P., Mazzitelli, G., Colafrancesco, S., & Vittorio, N. 1998, A&AS, 133, 403
Meng, X., Chen, X., & Han, Z. 2009, MNRAS, 395, 2103
Miceli, M., et al. 2009, A&A, 501, 239
Morrison, R., & McCammon, D. 1983, ApJ, 270, 119
Ossenkopf, V., Esquivel, A., Lazarian, A., & Stutzki, J. 2006, A&A, 452, 223
Pakmor, R., Röpke, F. K., Weiss, A., & Hillebrandt, W. 2008, A&A, 489, 943
Raga, A. C., De Colle, F., Kajdič, P., Esquivel, A., & Cantó, J. 2007, A&A, 465, 879
Raga, A. C., de Gouveia Dal Pino, E. M., Noriega-Crespo, A., Mininni, P. D., & Velázquez, P. F. 2002, A&A, 392, 267
Raga, A. C., Navarro-González, R., & Villagrán-Muniz, M. 2000, RevMexAA, 36, 67
Reyes-Iturbide, J., Rosado, M., & Velázquez, P. F. 2008, AJ, 136, 2011
Reynoso, E. M., Moffett, D. A., Goss, W. M., Dubner, G. M., Dickel, J. R., Reynolds, S. P., & Giacani, E. B. 1997, ApJ, 491, 816
Reynoso, E. M., Velázquez, P. F., Dubner, G. M., & Goss, W. M. 1999, AJ, 117, 1827
Ruiz-Lapuente, P., et al. 2004, Nature, 431, 1069
Schneiter, E. M., de La Fuente, E., & Velázquez, P. F. 2006, MNRAS, 371, 369
Schneiter, E. M., Velázquez, P. F., Reynoso, E. M., & De Colle, F. 2010, MNRAS, 408, 430
Schwarz, U. J., Goss, W. M., & Arnal, E. M. 1980, MNRAS, 192, 67

Schwarz, U. J., Goss, W. M., Kalberla, P. M., & Benaglia, P. 1995, A&A, 299, 193
Sedov, L. I. 1959, Similarity and Dimensional Methods in Mechanics (New York: Academic)
Smith, R. C., Kirshner, R. P., Blair, W. P., & Winkler, P. F. 1991, ApJ, 375, 652
Truelove, J. K., & McKee, C. F. 1999, ApJS, 120, 299
van Leer, B. 1982, Numerical Methods in Fluid Dynamics, Vol. 170 (Berlin: Springer), 507
Vancura, O., Gorenstein, P., & Hughes, P. 1995, ApJ, 441, 680
Velázquez, P. F., Vigh, C. D., Reynoso, E. M., Gómez, D. O., & Schneiter, E. M. 2006, ApJ, 649, 779
Warren, J. S., et al. 2005, ApJ, 634, 376
Wheeler, J. C., Lecar, M., & McKee, C. F. 1975, ApJ, 2001, 145
Woltjer, L. 1972, ARA&A, 10, 129
Zavala, J., Velázquez, P. F., Cerqueira, A. H., & Dubner, G. M. 2008, MNRAS, 387, 839